

# Noise Amplification in Parallel Whole-Head Ultra-Low-Field Magnetic Resonance Imaging Using 306 Detectors

Fa-Hsuan Lin,<sup>1,2\*</sup> Panu T. Vesänen,<sup>2</sup> Jaakko O. Nieminen,<sup>2</sup> Yi-Cheng Hsu,<sup>3</sup> Koos C.J. Zevenhoven,<sup>2</sup> Juhani Dabek,<sup>2</sup> Lauri T. Parkkonen,<sup>2</sup> Andrey Zhdanov,<sup>2</sup> and Risto J. Ilmoniemi<sup>2</sup>

In ultra-low-field magnetic resonance imaging, arrays of up to hundreds of highly sensitive superconducting quantum interference devices (SQUIDs) can be used to detect the weak magnetic fields emitted by the precessing magnetization. Here, we investigate the noise amplification in sensitivity-encoded ultra-low-field MRI at various acceleration rates using a SQUID array consisting of 102 magnetometers, 102 gradiometers, or 306 magnetometers and gradiometers, to cover the whole head. Our results suggest that SQUID arrays consisting of 102 magnetometers and 102 gradiometers are similar in *g*-factor distribution. A SQUID array of 306 sensors (102 magnetometers and 204 gradiometers) only marginally improves the *g*-factor. Corroborating with previous studies, the *g*-factor in 2D sensitivity-encoded ultra-low-field MRI with 9 to 16-fold 2D accelerations using the SQUID array studied here may be acceptable. **Magn Reson Med 70:595–600, 2013. © 2012 Wiley Periodicals, Inc.**

**Key words:** SENSE; *g*-factor; ultra-low-field MRI; magnetoencephalography; MEG-MRI; conjugated gradient; parallel MRI

MRI can noninvasively delineate human anatomical structures and functional activity with a high spatial resolution. Even with its great success in clinical medicine and biomedical research, MRI still faces significant challenges. First, a strong magnet is usually required to generate sufficiently large magnetization to be detected. The cost of a high-field magnet (1.5 T, 3 T, or even 7 T) constitutes a major part of the cost of an MRI system. Second, because of potential mechanical or electrical hazards, acquiring MR images from patients with metallic objects is difficult. However, imaging patients with

wounds caused by metallic objects or with interventional devices (e.g., in the intensive care unit or the emergency room) is clinically desirable.

Recently, methods of performing MRI at ultra-low-fields (ULFs) have been developed to mitigate challenges described above (for review, see Ref. 1). Different from commercially available “low-field” MRI with  $B_0 \approx 0.2$  T, ULF-MRI systems usually use magnetic field strength in the range of microteslas or milliteslas. ULF-MRI systems have the advantages of metal compatibility (2), low hardware cost, and high  $T_1$  contrast (3), which may allow accurate discrimination between healthy and cancerous tissue (4,5). However, the SNR in ULF MRI is poor because of limited magnetization. The challenge of low SNR at low field strengths can be mitigated by two approaches. First, magnetization is produced by a higher “prepolarizing field”  $B_p$ ; then, a lower “measurement field”  $B_m$  is applied separately to allow the desired magnetization precession. This is different from high-field MRI, where the same strong magnet is used for magnetization and magnetization precession. ULF-MRI systems have been demonstrated with  $B_p$  of the order of 10–100 mT and  $B_m$  in the 10–200  $\mu$ T range (6,7). Second, unlike high-field MRI with narrow-band tuned radiofrequency (RF) coils for signal excitation and reception, ULF MRI uses the highly sensitive superconducting quantum interference devices (SQUIDs) to detect the weak magnetic fields (8). The combination of these techniques makes the signal of a ULF system to be linearly proportional to the polarizing field and independent of the measurement field. These two techniques are not used in high-field MRI, because (1) a high field generates sufficient magnetization for signal detection, and (2) SQUIDs cannot tolerate the high-field environment (saturation effects).

The feasibility of measurement of ULF MRI and magnetoencephalography (MEG), a method to detect the weak magnetic fields generated by coherent postsynaptic currents in human brain, with a single device has also been demonstrated (9,10). This is particularly important for neuroscience research as in this case spatial registration is no more needed to combine anatomical and electrophysiological measurements. Despite this progress, ULF MRI is faced with a major technical challenge: the data acquisition is relatively inefficient: acquiring a  $9 \times 9$  cm<sup>2</sup> 2D image with a spatial resolution of 0.7 mm by 0.7 mm takes about 5 min (1). Specifically, more than 80% of the ULF-MRI acquisition is spent on magnetically polarizing the sample (11).

The MRI acquisition time can be shortened only fractionally by the echo-train technique or partial Fourier

<sup>1</sup>Institute of Biomedical Engineering, National Taiwan University, Taipei, Taiwan.

<sup>2</sup>Department of Biomedical Engineering and Computational Science, Aalto University School of Science, Espoo, Finland.

<sup>3</sup>Department of Mathematics, National Taiwan University, Taipei, Taiwan.

Grant sponsor: National Institutes of Health; Grant numbers: R01DA14178, R01HD040712, R01NS037462, R01NS048279, P41RR14075, R01EB006847, R01EB000790, R01MH083744, R21DC010060; Grant sponsor: National Center for Research Resources; Grant numbers: NSC 101-2628-B-002-005-MY3, NSC 100-2325-B-002-046 (National Science Council, Taiwan), 100-EC-17-A-19-S1-175 (Ministry of Economic Affairs, Taiwan); Grant sponsors: Academy of Finland (the FiDiPro program); Grant sponsor: European Community's Seventh Framework Programme; Grant number: 200859

\*Correspondence to: Fa-Hsuan Lin, Ph.D., Institute of Biomedical Engineering, National Taiwan University, 1 Sec. 4 Roosevelt Road, 106 Taipei, Taiwan. E-mail: fhlin@ntu.edu.tw

Received 19 May 2012; revised 9 August 2012; accepted 9 August 2012.

DOI 10.1002/mrm.24479

Published online 28 September 2012 in Wiley Online Library (wileyonlinelibrary.com).

acquisitions (12). More accelerated MRI acquisitions are made possible by the parallel MRI (pMRI) (13,14) method using RF array technology (15): by combining RF sensitivity information from, for example, a 32-channel RF coil head array, the data acquisition time can be reduced two-fold to fourfold without much sacrificed quality (16). An ULF-MRI study with a seven-channel SQUID system demonstrated the feasibility of threefold acceleration (11). pMRI achieves acceleration at the cost of signal-to-noise ratio (SNR) due to the loss of data samples and the reconstruction associated noise amplification (13). While the former loss is inevitable in acceleration, the latter loss can be compensated for by regularized reconstruction methods (17,18) and by increasing the number of parallel detectors. It has been shown that with many elements one can approach the ultimate performance. But even with many elements, at about fivefold acceleration in one dimension, the SNR efficiency is already half of that of the unaccelerated case (19,20).

In this article, we investigate the SNR penalty of accelerated ULF MRI. Specifically, we use the  $g$ -factor to quantify the relative SNR efficiency of accelerated ULF MRI at different acceleration rates and array geometries based on the empirically measured noise covariance matrix from a whole-head MEG system. The goal of this study is to quantitatively evaluate the  $g$ -factor distribution in accelerated ULF MRI. These numbers may suggest the acceptable noise amplification penalty and thus the acceleration rate, if ultimately the loss of SNR due to reduced number of samples is practically tolerable.

## METHODS

### Coil Arrays

In ULF MRI, broadband SQUIDs rather than narrow-band tuned RF coils are used as magnetic field detectors. When an ULF-MRI system is built around an existing modern MEG system, pMRI techniques can be realized using the multichannel SQUID sensor array geometry already available in the MEG system. These SQUID sensors are not spatially overlapping as there is no need to minimize the mutual inductance as in tuned RF coils in high-field MRI arrays (15). The number of SQUID sensors in a whole-head MEG system ranges from 122 to 306 (21). This exceeds the number of RF channels in present RF head coil arrays in high-field MRI with 32 (16), or maximally 96 channels (22). Body coil arrays with up to 128 channels have also been developed (23,24). While increasing the number of sensors indefinitely will eventually cause oversampling of data (only correlated rather than independent measurements are collected), a MEG system with 306 channels (102 units of combined one magnetometer and two gradiometers) is still within a reasonable range (25).

We studied an array geometry designed to allow 102 elements to cover the whole head evenly, based on a 306-channel MEG system (VectorView, Elekta Oy, Helsinki, Finland). Specifically, we used either 102 channels of magnetometers (planar circular loops, denoted as array102), 102 channels of gradiometers (planar figure-eight loops, denoted as array102x or array102y), or the combination of both (denoted as array306) to cover the whole head. These arrays are shown in Figure 1.

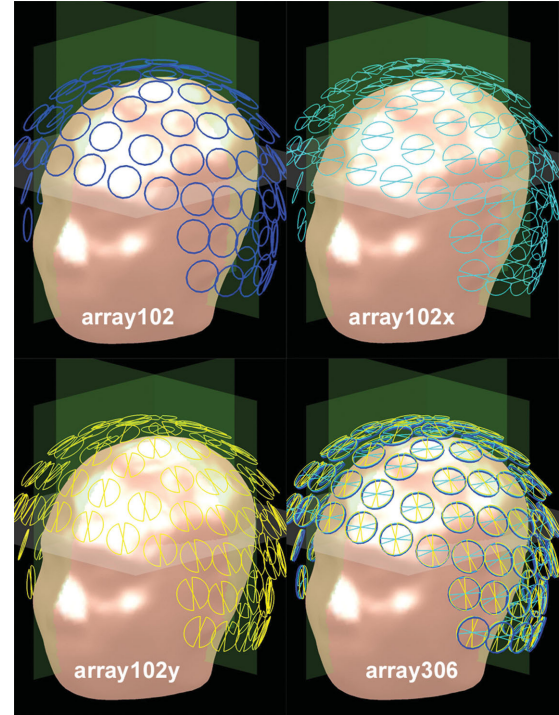


FIG. 1. The geometries of the arrays of 102 or 306 pick-up coils to cover the whole head. Each pick-up coil can be a circular loop similar to the “magnetometer” in MEG (array102), a figure-eight loop similar to the “gradiometer” in MEG (array102x and array102y), or the combination of both (array306). Orthogonal slices for  $g$ -factor calculation are illustrated by translucent planes. [Color figure can be viewed in the online issue, which is available at [wileyonlinelibrary.com](http://wileyonlinelibrary.com).]

### $g$ -Factor Calculation

Given a coil array geometry, we used the Biot–Savart law to calculate the magnetic fields generated by a unit coil current on each element separately. As our system has the measurement field  $B_m$  oriented along the  $y$ -axis, the  $x$ - $z$  plane will be the plane of the rotating magnetization. Figure 2 shows our ULF-MRI setup. Details of this system have been described in Ref. 10. Accordingly, the magnetic field components in the  $x$  and  $z$  directions consist of the real and imaginary parts of the coil sensitivity maps. However, with our measurement-field  $B_m$  coils, consisting of two pairs of equiplanar square coils, the measurement field is not exactly aligned along the  $y$ -axis over the 256-mm field of view (FOV). Therefore, we defined the metrics  $h_x$ ,  $h_z$ , and  $h_{xz}$  to quantify how much  $B_m$  deviates from the  $y$ -axis:

$$\begin{aligned} h_x(\vec{r}) &= |B_x^g(\vec{r})|/|B_y^g(\vec{r})| \\ h_z(\vec{r}) &= |B_z^g(\vec{r})|/|B_y^g(\vec{r})| \\ h_{xz}(\vec{r}) &= \sqrt{B_x^g(\vec{r})^2 + B_z^g(\vec{r})^2}/|B_y^g(\vec{r})|^2 \end{aligned} \quad [1]$$

Here,  $B_x^g(\vec{r})$ ,  $B_y^g(\vec{r})$ , and  $B_z^g(\vec{r})$  represent the  $x$ -,  $y$ -, and  $z$ -components of the magnetic field at location  $\vec{r}$

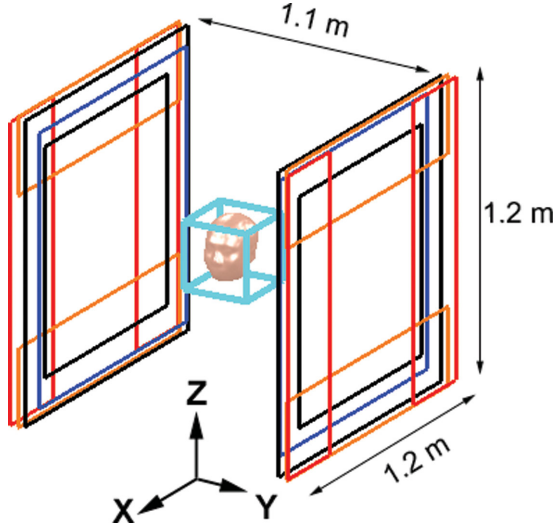


FIG. 2. The setup of ULF MRI. Two pairs of square coils (black) generate the measurement field. Gradient coils in the  $x$  and  $z$  directions are two pairs of loops colored red and orange, respectively. The gradient coils in the  $y$  direction consist of the two blue loops. A volumetric FOV of 256 mm is shown by the cyan box at the center of the ULF-MRI setup. [Color figure can be viewed in the online issue, which is available at [wileyonlinelibrary.com](http://wileyonlinelibrary.com).]

generated by two pairs of equiplanar square coils, respectively. Ideally,  $h_x(\vec{r})$ ,  $h_z(\vec{r})$ , and  $h_{xz}(\vec{r})$  should be 0, that is,  $B_m$  aligned exactly with the  $y$ -axis.

In sensitivity-encoded pMRI formulation, the  $g$ -factor accounts for the relative SNR efficiency during an accelerated scan (13):

$$\frac{\text{SNR}_p^{\text{accelerated}}}{\text{SNR}_p^{\text{full}}} = \frac{1}{g_p \sqrt{R}} \quad [2]$$

$$g_p = \sqrt{[(\mathbf{E}^H \Psi^{-1} \mathbf{E})^{-1}]_{p,p} (\mathbf{E}^H \Psi^{-1} \mathbf{E})_{p,p}}$$

The subscript  $p$  indicates the voxel to be reconstructed, and the superscript  $H$  denotes the conjugate transpose.  $R$  denotes the factor by which the number of samples is reduced (the acceleration rate). The encoding matrix  $\mathbf{E}$  consists of the product of the aliasing operation due to subsampling of the  $k$ -space data and complex-valued coil-

sensitivity maps.  $\Psi$  is the receiver noise covariance matrix across channels of the receiver array. The double subscript  $p,p$  denotes the diagonal element at location  $p$ . In this study,  $\Psi$  was empirically measured from a whole-head MEG system (VectorView, Elekta Oy, Helsinki, Finland) with 306 SQUID sensors as described in Figure 1. The measurement for noise covariance matrix had 1000-Hz sampling rate and its duration was 5 min with a subject inside the MEG shielded room with the subject's eyes open during the measurement, in order to suppress spontaneous alpha oscillation. This measurement was further high-pass filtered at 100 Hz in order to suppress spontaneous brain activity in beta and gamma bands to avoid spurious coupling between sensors in the noise covariance matrix estimation.

We first studied the spatial distribution of the SNR of different coil array geometries. Specifically, the SNR map is related to the magnetic fields and the noise covariance matrix  $\Psi$ :

$$\text{SNR}_p(\vec{r}) \propto \sqrt{(B_{xz}^H(\vec{r}) \Psi^{-1} B_{xz}(\vec{r}))_{p,p}}$$

$$B_{xz}^c(\vec{r}) = B_x^c(\vec{r}) + j B_z^c(\vec{r}) \quad [3]$$

$$B_{xz}(\vec{r}) = \begin{bmatrix} B_{xz}^1(\vec{r}) \\ \vdots \\ B_{xz}^{n_c}(\vec{r}) \end{bmatrix}$$

where  $B_x^c(\vec{r})$  and  $B_z^c(\vec{r})$  denotes the  $x$ - and  $z$ -component of the magnetic field at location  $\vec{r}$  for channel  $c$  respectively, and  $n_c$  is the number of channels. As  $B_x^c(\vec{r})$  and  $B_z^c(\vec{r})$  were calculated based on array the geometry and  $\Psi$  was empirically measured, we arbitrarily scaled the maximum SNR of the array 102 to be 100.

In this study, we targeted on acceleration in two dimensions (along the  $x$ - and  $y$ -axes; Figure 2), since the spatial arrangement of the channels was approximately symmetric in the horizontal plane. Such an acquisition can be realized in 3D MRI pulse sequences with two phase encoding directions along the  $x$ - and  $y$ -axes and the frequency encoding along the  $z$  direction. We calculated  $g$ -factor maps at  $R = 2 \times 2, 3 \times 3, 4 \times 4, 6 \times 6, 8 \times 8$ , and  $10 \times 10$ , as more channels allow a higher acceleration rate. The spatial distribution of the  $g$ -factor was calculated at the mid-sagittal slice, the mid-coronal slice, and a transverse slice approximately above the eye brows. We

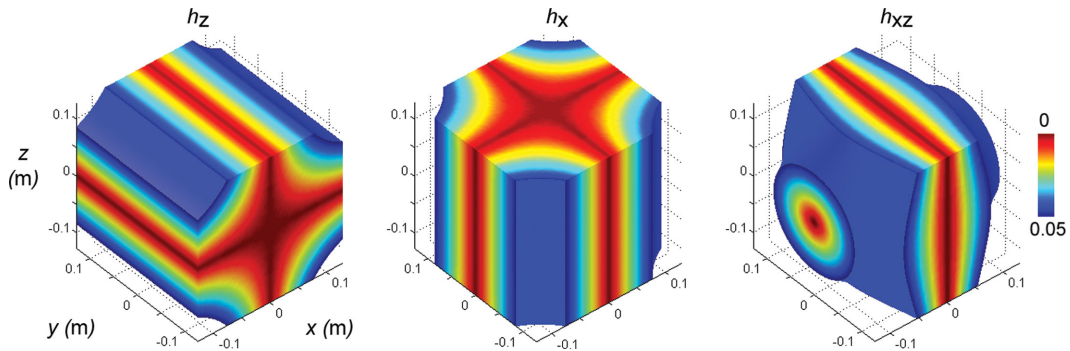


FIG. 3. The spatial distribution of the  $h_z$ ,  $h_x$ , and  $h_{xz}$  indices describing the deviation of the measurement field away from the  $y$ -axis. Only regions smaller than 0.05 (less than  $2.9^\circ$  from the  $y$ -axis) were color coded within the 256-mm FOV. [Color figure can be viewed in the online issue, which is available at [wileyonlinelibrary.com](http://wileyonlinelibrary.com).]



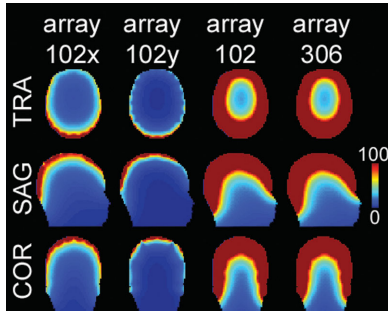


FIG. 4. The spatial distribution of SNR in mid-sagittal, mid-coronal, and one axial slice with array102, array102x, array102y, and array306 geometries.

reported the average, standard deviation, the maximum, and the minimum of  $g$ -factors in our calculation.

The simulations were implemented by MatLab (Mathworks, Natick, MA) on a workstation with Intel 2.0 GHz Xeon CPU and 32 Gbytes memory. Calculations for all coil arrays and all acceleration rates used an image matrix of size  $64 \times 64 \times 64$ . A digital head phantom was created from high-resolution 3D  $T_1$ -weighted structural MRI data acquired on a 3T MRI scanner using the MPRAGE pulse sequence (pulse repetition time/echo time/flip angle = 2530 ms/3.49 ms/7°, partition thickness = 1.0 mm, matrix =  $256 \times 256$ , 256 partitions, FOV =  $256 \text{ mm} \times 256 \text{ mm}$ ).

## RESULTS

Figure 3 shows the spatial distribution of  $h_z$ ,  $h_x$ , and  $h_{xz}$  within the 256-mm FOV. Most of the volume was covered with  $h_z$ ,  $h_x$ , and  $h_{xz}$  smaller than 0.05, which equals a deviation of the measurement field ( $B_m$ ) of 2.9 degrees or less from the  $y$ -axis. This result suggests that over this FOV the magnetization precession plane is dominantly

at the  $x$ - $z$  plane and thus the  $x$ - and  $z$ -components of the magnetic fields of each pick-up coil can constitute the effective  $B_1$  field maps.

Figure 4 shows the spatial distribution of the full SNR for different array geometries. All geometries have high SNR close to the scalp. Particularly, the array using gradiometers (array 102x and array 102y) shows very fast decay of the SNR profile as the location is away from the scalp. This is because the gradiometers take the spatial derivative of the measurements and thus they are exquisitely sensitive to the cortical signal (21). This calculation was found consistent with a previous study (21). The difference between arrays using magnetometers (array 102 and array 306) was visually indistinguishable.

Figure 5 shows the spatial distribution of  $1/g$  at  $R = 2 \times 2$ ,  $3 \times 3$ ,  $4 \times 4$ ,  $6 \times 6$ ,  $8 \times 8$ , and  $10 \times 10$  over the FOV of  $256 \text{ mm} \times 256 \text{ mm} \times 256 \text{ mm}$ . An increased  $g$ -factor penalty was observed at a higher acceleration rate. The  $g$ -factor is smaller (showing a higher  $1/g$  value) at superficial locations in all acceleration rates. The average, standard deviation, maximum, and minimum of  $g$ -factors are reported in Table 1. Interestingly, arrays with gradiometer pick-up coils (array102x or array102y) show a similar  $g$ -factor distribution to the array with magnetometer pick-up coils (array102). A combination of both gradiometer and magnetometer pick-up coils (array306) can slightly improve the  $g$ -factor at image locations closer to the array elements. In all geometries, image locations away from pick-up coils show a larger  $g$ -factor in general.

## DISCUSSION

We investigated the noise amplification penalty in accelerated ULF MRI quantified by the  $g$ -factor in four different whole-head SQUID sensor array geometries. Using the same number of SQUID pick-up coils, we found that there is no clear difference between arrays using magnetometers and gradiometers. An array using 306

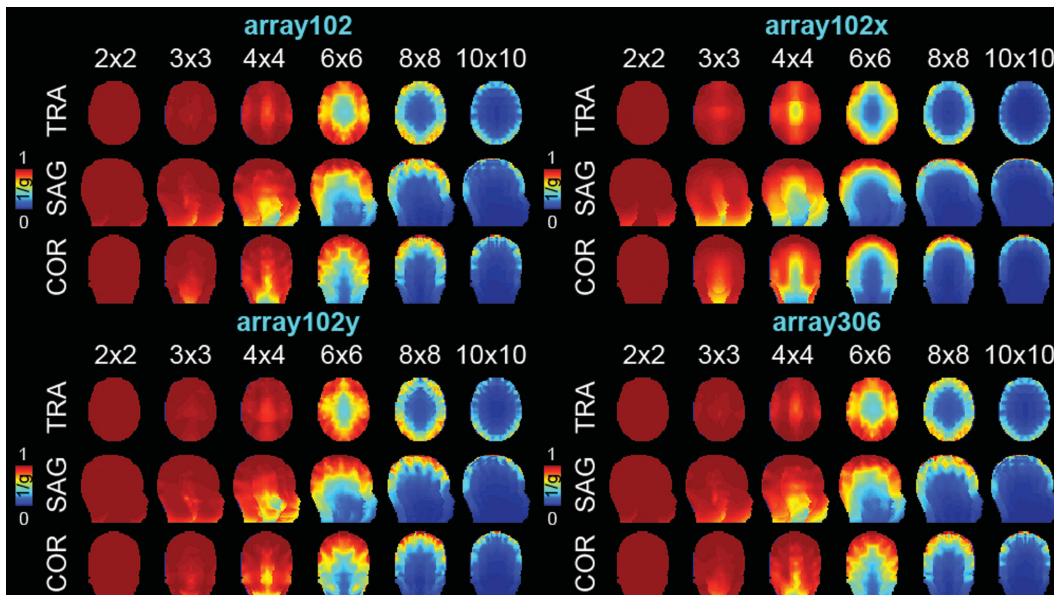


FIG. 5. The spatial distribution of  $1/g$ -factor in mid-sagittal, mid-coronal, and one axial slice with array102, array102x, array102y, and array306 geometries at  $R = 2 \times 2$ ,  $3 \times 3$ ,  $4 \times 4$ ,  $6 \times 6$ ,  $8 \times 8$ , and  $10 \times 10$  over the FOV of  $256 \text{ mm} \times 256 \text{ mm} \times 256 \text{ mm}$ .

Table 1

Average, Standard Deviation, Maximum, and Minimum of  $g$ -Factors in array102 (A), array102x (B), array102y (C), and array306 (D)

(A) Acceleration rate ( $R$ )	$2 \times 2$	$3 \times 3$	$4 \times 4$	$6 \times 6$	$8 \times 8$	$10 \times 10$
Average	1.0	1.1	1.1	1.9	6.9	29.0
Standard deviation	0.0	0.0	0.2	1.1	9.4	50.8
Max	1.1	1.5	2.9	11.9	113.2	468.1
Min	1.0	1.0	1.0	1.0	1.0	1.0
(B) Acceleration rate ( $R$ )	$2 \times 2$	$3 \times 3$	$4 \times 4$	$6 \times 6$	$8 \times 8$	$10 \times 10$
Average	1.0	1.1	1.3	3.3	17.0	66.1
Standard deviation	0.0	0.1	0.4	3.0	28.0	105.7
Max	1.2	2.1	4.8	32.6	312.6	828.0
Min	1.0	1.0	1.0	1.0	1.0	1.0
(C) Acceleration rate ( $R$ )	$2 \times 2$	$3 \times 3$	$4 \times 4$	$6 \times 6$	$8 \times 8$	$10 \times 10$
Average	1.0	1.0	1.1	2.0	7.6	30.4
Standard deviation	0.0	0.0	0.2	1.2	10.7	49.4
Max	1.1	1.5	2.6	14.2	124.7	529.8
Min	1.0	1.0	1.0	1.0	1.0	1.0
(D) Acceleration rate ( $R$ )	$2 \times 2$	$3 \times 3$	$4 \times 4$	$6 \times 6$	$8 \times 8$	$10 \times 10$
Average	1.0	1.0	1.1	1.9	6.9	29.0
Standard deviation	0.0	0.0	0.2	1.1	9.3	50.6
Max	1.1	1.5	2.6	11.7	111.8	462.0
Min	1.0	1.0	1.0	1.0	1.0	1.0

gradiometers and magnetometers only slightly improves the  $g$ -factors. In a 3D MRI acquisition with two phase encoding directions, the highest acceptable acceleration rate suggested by the average  $g$ -factor may range between 9- and 16-fold (using an arbitrary threshold of average  $g$ -factor = 1.4). This  $g$ -factor calculation was in fact consistent with previous high-field MRI studies using electromagnetic dynamics (26) and empirical validation at high field (27). In ULF MRI, most of the time is spent on preparing the magnetization. A 3D acquisition with  $64 \times 64 \times 64$  voxels needs 4,096 independent measurements. With pulse repetition time = 1 s, this amounts to more than an hour of acquisition time. Using a coil array of 102 elements and ninefold acceleration, when ignoring the SNR loss due to reduced samples, the data acquisition can be completed in approximately 7 min. However, as suggested by our results, spatially varying noise amplifications (i.e.,  $g$ -factor) could be significant at 9- and 16-fold acceleration, resulting in inhomogeneous image quality deterioration.

It is important to remember that SNR always degrades as the number of data samples is reduced. The  $g$ -factor = 1 condition only ensures that no additional noise is introduced in the image reconstruction, while the SNR still becomes, for example, 1/3 in ninefold acceleration (13). Such an SNR penalty may not be tolerable in ULF MRI with the present instrumentation. Yet, with the increasing prepolarization to obtain stronger magnetization and with more sensitive SQUIDs to minimize noise, trading off SNR for a faster data acquisition rate may be feasible in future ULF MRI.

Low  $g$ -factor penalty may suggest repeating accelerated ULF-MRI acquisitions such that the total number of data samples, and thus the SNR, approximates the unaccelerated acquisition. One benefit of this approach is that images can be acquired in a shorter interval to minimize motion artifacts. Specifically, when transient motion occurs, only a small fraction of data needs to be discarded. Images can be reconstructed and averaged from

multiple intact accelerated acquisitions. As the noise amplification is minimal, the final image still has comparable SNR as the unaccelerated acquisition. Without doing this, a transient motion artifact can deteriorate the whole data acquisition, which is a considerable risk as the ULF MRI can take more than one hour with present technology.

In our calculations, we explicitly ignored the magnetic fields from the gradient coils, which can further deviate the measurement field away from the  $y$ -axis, depending on the time diagram of each gradient coil element. In fact, gradient coils produce concomitant fields and make a notable image distortion in ULF MRI (28–31). Considering a gradient strength of 100  $\mu\text{T/m}$  in 2D imaging (11), there should be a field of 12.8  $\mu\text{T}$  at the boundary of a 256-mm FOV. The measurement field in our system was designed to have a Larmor frequency of 2000 Hz, corresponding to 47.0  $\mu\text{T}$ . Supposing the concomitant field strength in the  $x$  and  $z$  directions is about the same magnitude as in the  $y$  direction, these numbers suggest that the measurement field will deviate  $15^\circ$ . At such an angle, we may still use  $x$ - and  $z$ -components of the magnetic field in a pick-up coil for  $B_1$  sensitivity.

Our calculations show that an array of 102 SQUID pick-up coils may be sufficient to minimize the  $g$ -factor. However, for a hybrid system targeting at measuring both MEG and ULF MRI (9), an array of 204 gradiometers and 102 magnetometers may be still desirable for MEG measurements. This is the target of our prototype system.

## REFERENCES

- Clarke J, Hatridge M, Mölle M. SQUID-detected magnetic resonance imaging in microtesla fields. *Annu Rev Biomed Eng* 2007;9: 389–413.
- Mölle M, Han SI, Myers WR, Lee SK, Kelso N, Hatridge M, Pines A, Clarke J. SQUID-detected microtesla MRI in the presence of metal. *J Magn Reson* 2006;179:146–151.
- Lee SK, Mölle M, Myers W, Kelso N, Trabesinger AH, Pines A, Clarke J. SQUID-detected MRI at 132 mT with T1-weighted contrast established at 10  $\mu\text{T}$ –300  $\mu\text{T}$ . *Magn Reson Med* 2005;53:9–14.

4. Liao S-H, Huang K-W, Yang H-C, Yen C-T, Chen M-J, Chen H-H, Horng H-E, Yang S-Y. Characterization of tumors using high-Tc superconducting quantum interference device-detected nuclear magnetic resonance and imaging. *Appl Phys Lett* 2010;97:263701–263703.
5. Busch S, Hatridge M, Möble M, Myers W, Wong T, Muck M, Chew K, Kuchinsky K, Simko J, Clarke J. Measurements of  $T_1$ -relaxation in ex vivo prostate tissue at 132  $\mu$ T. *Magn Reson Med* 2012;67:1138–1145.
6. McDermott R, Lee S, ten Haken B, Trabesinger AH, Pines A, Clarke J. Microtesla MRI with a superconducting quantum interference device. *Proc Natl Acad Sci USA* 2004;101:7857–7861.
7. Matlachov AN, Volegov PL, Espy MA, George JS, Kraus RH, Jr. SQUID detected NMR in microtesla magnetic fields. *J Magn Reson* 2004;170:1–7.
8. McDermott R, Lee S, ten Haken B, Trabesinger AH, Pines A, Clarke J. Microtesla MRI with a superconducting quantum interference device. *Proc Natl Acad Sci USA* 2004;101:7857–7861.
9. Zotev VS, Matlachov AN, Volegov PL, Savukov IM, Espy MA, Mosher JC, Gomez JJ, Kraus RH, Jr. Microtesla MRI of the human brain combined with MEG. *J Magn Reson* 2008;194:115–120.
10. Vesanen PT, Nieminen JO, Zevenhoven KCJ, et al. Hybrid ultra-low-field MRI and MEG system based on a commercial whole-head neuromagnetometer. *Magn Reson Med* 2013;69:1795–1804.
11. Nenonen J, Taulu S, Kajola M, Ahonen A. Total information extracted from MEG measurements. *Int Congr Ser* 2007;1300:245–248.
12. Zotev VS, Volegov PL, Matlachov AN, Espy MA, Mosher JC, Kraus RH, Jr. Parallel MRI at microtesla fields. *J Magn Reson* 2008;192:197–208.
13. Bernstein MA, King KF, Zhou XJ. *Handbook of MRI pulse sequences*. Amsterdam; Boston: Academic Press; 2004. xxii, 1017 pp.
14. Pruessmann KP, Weiger M, Scheidegger MB, Boesiger P. SENSE: sensitivity encoding for fast MRI. *Magn Reson Med* 1999;42:952–962.
15. Sodickson DK, Manning WJ. Simultaneous acquisition of spatial harmonics (SMASH): fast imaging with radiofrequency coil arrays. *Magn Reson Med* 1997;38:591–603.
16. Roemer PB, Edelstein WA, Hayes CE, Souza SP, Mueller OM. The NMR phased array. *Magn Reson Med* 1990;16:192–225.
17. Wiggins GC, Triantafyllou C, Potthast A, Reykowski A, Nittka M, Wald LL. 32-channel 3 Tesla receive-only phased-array head coil with soccer-ball element geometry. *Magn Reson Med* 2006;56:216–223.
18. Lin FH, Huang TY, Chen NK, Wang FN, Stufflebeam SM, Belliveau JW, Wald LL, Kwong KK. Functional MRI using regularized parallel imaging acquisition. *Magn Reson Med* 2005;54:343–353.
19. Lin FH, Kwong KK, Belliveau JW, Wald LL. Parallel imaging reconstruction using automatic regularization. *Magn Reson Med* 2004;51:559–567.
20. Lattanzi R, Grant AK, Sodickson DK. Approaching ultimate SNR and ideal current patterns with finite surface coil arrays on a dielectric cylinder. In *Proceedings of the 16th Annual Meeting of ISMRM*, Toronto, Canada, 2008. p. 1074.
21. Wiesinger F, De Zanche N, Pruessmann KP. Approaching ultimate SNR with finite coil arrays. In *Proceedings of the 13th Annual Meeting of ISMRM*, Miami, Florida, USA, 2005. p. 672.
22. Hämäläinen M, Hari R, Ilmoniemi RJ, Knuutila J, Lounasmaa OV. Magnetoencephalography-theory, instrumentation, and application to noninvasive studies of the working human brain. *Rev Mod Phys* 1993;65:413–497.
23. Wiggins GC, Polimeni JR, Potthast A, Schmitt M, Alagappan V, Wald LL. 96-Channel receive-only head coil for 3 Tesla: design optimization and evaluation. *Magn Reson Med* 2009;62:754–762.
24. Hardy CJ, Giaquinto RO, Piel JE, Rohling KW, Marinelli L, Blezek DJ, Fiveland EW, Darrow RD, Foo TK. 128-channel body MRI with a flexible high-density receiver-coil array. *J Magn Reson Imaging* 2008;28:1219–1225.
25. Schmitt M, Potthast A, Sosnovik DE, Polimeni JR, Wiggins GC, Triantafyllou C, Wald LL. A 128-channel receive-only cardiac coil for highly accelerated cardiac MRI at 3 Tesla. *Magn Reson Med* 2008;59:1431–1439.
26. Wiesinger F, Boesiger P, Pruessmann KP. Electrodynamics and ultimate SNR in parallel MR imaging. *Magn Reson Med* 2004;52:376–390.
27. Wiesinger F, Van de Moortele PF, Adriany G, De Zanche N, Ugurbil K, Pruessmann KP. Parallel imaging performance as a function of field strength—an experimental investigation using electrodynamic scaling. *Magn Reson Med* 2004;52:953–964.
28. Myers WR, Möble M, Clarke J. Correction of concomitant gradient artifacts in experimental microtesla MRI. *J Magn Reson* 2005;177:274–284.
29. Nieminen JO, Ilmoniemi RJ. Solving the problem of concomitant gradients in ultra-low-field MRI. *J Magn Reson* 2010;207:213–219.
30. Volegov PL, Mosher JC, Espy MA, Kraus RH, Jr. On concomitant gradients in low-field MRI. *J Magn Reson* 2005;175:103–113.
31. Yablonskiy DA, Sukstanskii AL, Ackerman JJ. Image artifacts in very low magnetic field MRI: the role of concomitant gradients. *J Magn Reson* 2005;174:279–286.